Numerical relativity higher order gravitational waveforms of eccentric, spinning, nonprecessing binary black hole mergers

Abhishek V. Joshi,[1,2,*] Shawn G. Rosofsky,[1,2] Roland Haas,[1,2] and E. A. Huerta[3,4,2]

[1]NCSA, University of Illinois at Urbana-Champaign, Urbana, Illinois 61801, USA
[2]Department of Physics, University of Illinois at Urbana-Champaign, Urbana, Illinois 61801, USA
[3]Data Science and Learning Division, Argonne National Laboratory, Lemont, Illinois 60439, USA
[4]Department of Computer Science, University of Chicago, Chicago, Illinois 60637, USA

(Received 6 October 2022; accepted 24 February 2023; published 20 March 2023)

We use the open source, community-driven, numerical relativity software, the EINSTEIN TOOLKIT to study the physics of eccentric, spinning, nonprecessing binary black hole mergers with mass-ratios $q = \{2, 4, 6\}$, individual dimensionless spin parameters $\chi_{1z} = \pm 0.6$, $\chi_{2z} = \pm 0.3$, that include higher order gravitational wave modes $\ell \leq 4$, except for memory modes. Assuming stellar mass binary black hole mergers that may be detectable by the advanced LIGO detectors, we find that including modes up to $\ell = 4$ increases the signal-to-noise of compact binaries between 3.5% to 35%, compared to signals that only include the $\ell = |m| = 2$ mode. We use two waveform models, TEOBResumS and SEOBNRE, which incorporate spin and eccentricity corrections in the waveform dynamics, to quantify the orbital eccentricity of our numerical relativity catalog in a gauge-invariant manner through fitting factor calculations. Our findings indicate that the inclusion of higher order wave modes has a measurable effect in the recovery of moderately and highly eccentric black hole mergers, and thus it is essential to develop waveform models and signal processing tools that accurately describe the physics of these astrophysical sources.

DOI: 10.1103/PhysRevD.107.064038

I. INTRODUCTION

The modeling of eccentric compact binary mergers has attracted significant attention in recent years. The understanding of these astrophysical sources has gradually increased through a variety of analytical and numerical relativity studies that have shed new light into physics of these systems, and the properties of the gravitational wave signals that may be emitted by these sources [1–32]. Strides in the modeling and understanding of eccentric compact binary mergers has been accompanied by population synthesis models [33–36] that have been significantly improved to be compatible with the observation of stellar mass black holes in dense stellar environments, such as globular clusters in our galaxy [37–39], and galactic nuclei [40–42].

Impelled by these theoretical and observational advances, researchers have developed the required tools to search for this astrophysical population in gravitational wave data [43–48]. Some recent studies have attempted to constrain the eccentricity of actual gravitational wave sources [49]. A plethora of studies for the massive stellar black hole merger named GW190521 [50] provide persuasive evidence for the existence of eccentric compact binary mergers in dense stellar environments [28,51,52]. It is expected that several tens of eccentric compact binary mergers observed by advanced ground-based gravitational wave detectors will suffice to understand what formation channels contribute or dominate the eccentric merger rate [49].

In view of these developments, and the upcoming deluge of gravitational wave observations to be enabled by advanced LIGO [53,54] and its international counterparts VIRGO and KAGRA [47,55,56], it is timely and relevant to continue developing adequate tools for the identification of gravitational wave signals that may be produced by eccentric compact binary mergers.

The best tool at hand to gain insights about the physics of eccentric binary black hole mergers is numerical relativity, and thus we use the open source, community-driven, numerical relativity software, the EINSTEIN TOOLKIT [57] to produce a suite of numerical relativity waveforms that describe eccentric, spinning, nonprecessing binary black hole mergers. Non-spinning, eccentric simulations were investigated in previous works in [3,46]. These waveforms include higher order modes up to $\ell \leq 4$, except for memory modes. We use these numerical relativity waveforms to carry out the following studies:

(i) *Gravitational wave detection* We construct two types of waveforms that include either quadrupole

*avjoshi2@illinois.edu

modes, $\ell = |m| = 2$, or modes up to $\ell \leq 4$. We assume stellar mass binary black holes that may be observed by advanced LIGO-type detectors and compute signal-to-noise ratio (SNR) calculations for a variety of astrophysical scenarios, and explore whether the inclusion of higher order wave modes leads to measurable SNR increases.

(ii) *Gravitational wave modeling* We use two effective-one-body (EOB) eccentric waveform models: `TEOBResumS` [58–65] and `SEOBNRE` [5,66,67] to estimate the eccentricities of our numerical relativity waveforms. This exercise was useful to identify areas of improvement for next generation waveform models, and to get a better understanding of signals that may be discovered in upcoming gravitational wave searches. Note that due to conventions and different definitions of eccentricity, the inferred eccentricities cannot be directly compared with each other. A detailed comparison between the two waveform models is given in Knee *et al.* [68].

(iii) *Parameter space degeneracy* We quantified the impact of including higher order modes in terms of fitting factor calculations that aim to pinpoint an optimal quasicircular NRHybSur3dq8 waveform signal [69] whose astrophysical parameters best reproduce the complex morphology of moderately or highly eccentric numerical relativity waveforms.

These three complementary studies underscore the importance of improving our understanding of compact binary mergers in dense stellar environments. It is not enough to hope for the best and expect that burst or machine learning searches identify complex signals in gravitational wave data [46,48]. It is also necessary to develop a comprehensive toolkit that encompasses numerical relativity waveforms, semianalytical or machine learning based models, and signal processing tools to detect and then infer the astrophysical properties of eccentric compact binary mergers. Not doing so would be a disservice to the proven detection capabilities of advanced gravitational wave detectors, and would limit the science reach of gravitational wave astrophysics. To contribute to this important endeavor, we release our catalog of numerical relativity waveforms along with this article.

This article is organized as follows. We describe our approach to create a catalog of eccentric numerical relativity waveforms in Sec. II. Section IV presents our waveform catalog, and a systematic study on the importance of including higher order wave modes in terms of SNR calculations. In Sec. V we study whether surrogate models based on quasicircular, spinning, nonprecessing binary black hole numerical relativity waveforms can capture the physics of spinning, nonprecessing eccentric mergers. We summarize our findings and future directions of work in Sec. VI.

II. NUMERICAL SETUP AND SIMULATION DETAILS

We used the EINSTEIN TOOLKIT to generate a catalog of numerical relativity waveforms. Initial data for the binaries was computed using the TwoPunctures code. The evolution was done with the CTGAMMA code implementing the $3+1$ BSSN formulation. The outer boundary of the simulation domain was placed far enough (2500 M) to avoid any contamination of the signal until 200 M after the merger. Each simulation was run at three resolutions to check for convergence (see appendix A): $N = 36, 40, 44$ where N is the resolution across the finest grid radius. The highest resolution simulations were used for all analyses. Further details of the simulation setup are given in [3]. Waveforms extracted at future null infinity were computed for $1 < l \leq 4$ and $1 \leq |m| \leq l$ modes using the POWER code [70] by extrapolating the observed signals from 7 detectors located 100–700 M. $m = 0$ modes were not used since these modes (so-called memory modes) are many orders of magnitude smaller than the dominant modes of the waveform making a reliable estimation difficult due to numerical resolution (for more details see Sec. 6.2 in [71]). A plot of all the h_+ simulation waveforms is shown in Fig. 1. Note that the simulations are also dimensionalized in units of M.

Table I describes the properties of our waveform catalog, including the mass-ratio, individual spins and orbital eccentricity of each binary (measured from both waveform templates). The library consists of 27 simulations across 3 mass ratios, $q = \{2, 4, 6\}$, and a combination of nonprecessing individual spins, namely ± 0.6 and ± 0.3, for the primary (heavier) and secondary (lighter) binary components, respectively.

III. ECCENTRICITY MEASUREMENTS

Orbital eccentricity in a Keplerian interpretation can only be defined for a BBH system during the early inspiral, where the orbits of the binaries are nearly closed (the adiabatic approximation). This definition breaks down close to the merger, which is when our simulations begin. Thus, the definitions of eccentricity used to generate the initial conditions are ill-defined, even though they produce eccentric simulations.

Using evolution information of the binary, such as the separation between the components, throughout the simulation to obtain a measure of orbital eccentricity is not useful, as such a concept is gauge-dependent by assuming a coordinate system. To obtain a useful measure of eccentricity, we calibrate our numerical simulations to the spin-aligned eccentric EOB models `TEOBResumS` and `SEOBNRE`. For both of these models, a reference eccentricity e_0 and reference GW frequency $f_{\rm ref}$ are used as inputs to generate adiabatic initial conditions of the binary from which the waveform is computed. As investigated in Knee

TABLE I. *Physical parameters of numerical relativity waveform catalog* Mass-ratio, q, individual spins, (χ_{1z},χ_{2z}), and estimated orbital eccentricity, e_0, of our numerical relativity waveforms.

Simulation	q	χ_{1z}	χ_{2z}	TEOBResumS e_0(FF)	SEOBNRE e_0(FF)	$\chi_{\rm up}$
U1007	2	0.6	0.3	0.36 (97.2%)	0.39 (94.8%)	0.39
U1008	2	−0.6	−0.3	0.39 (98.3%)	0.67 (94.0%)	−0.39
U0009	2	0.6	0.3	0.46 (97.2%)	0.70 (29.3%)	0.39
U0010	2	−0.6	−0.3	0.47 (88.5%)	0.79 (99.3%)	−0.39
U0011	2	0.6	0.3	0.46 (55.6%)	0.08 (45.7%)	0.39
U0027	2	0.6	−0.3	0.47 (99.0%)	0.70 (90.3%)	0.26
U0028	2	−0.3	−0.3	0.40 (98.7%)	0.66 (96.7%)	−0.23
U0030	2	−0.3	−0.3	0.56 (76.7%)	0.77 (84.0%)	−0.23
U0014	4	−0.6	−0.3	0.27 (99.4%)	0.26 (99.8%)	−0.46
U1013	4	0.6	0.3	0.29 (97.5%)	0.33 (61.2%)	0.46
U1014	4	−0.6	−0.3	0.48 (98.3%)	0.68 (95.0%)	−0.46
U0015	4	0.6	0.3	0.47 (99.5%)	0.05 (28.7%)	0.46
U0017	4	0.6	0.3	0.56 (93.4%)	0.45 (30.2%)	0.46
U0032	4	−0.3	−0.3	0.40 (99.2%)	0.40 (87.2%)	−0.25
U0033	4	0.6	−0.3	0.44 (97.6%)	0.69 (18.6%)	0.39
U0034	4	−0.3	−0.3	0.40 (98.7%)	0.41 (93.1%)	−0.25
U0035	4	0.6	−0.3	0.56 (79.2%)	0.49 (25.7%)	0.39
U0036	4	−0.3	−0.3	0.44 (91.7%)	0.70 (79.7%)	−0.25
U0020	6	−0.6	−0.3	0.34 (99.7%)	N/A	−0.50
U1019	6	0.6	0.3	0.34 (94.9%)	0.58 (12.7%)	0.50
U1020	6	−0.6	−0.3	0.54 (93.8%)	N/A	−0.5
U0021	6	0.6	0.3	0.50 (93.7%)	0.20 (15.6%)	0.50
U0023	6	0.6	0.3	0.52 (98.4%)	0.60 (13.1%)	0.50
U0038	6	−0.3	−0.3	0.48 (97.3%)	0.70 (94.1%)	−0.26
U0039	6	0.6	−0.3	0.44 (96.2%)	0.26 (29.8%)	0.45
U0040	6	−0.3	−0.3	0.32 (98.3%)	0.41 (96.2%)	−0.26
U0041	6	0.6	−0.3	0.53 (96.8%)	0.47 (13.6%)	0.45

et al. [68], each waveform model's definition of e_0 may vary, due to different conventions of $f_{\rm ref}$ and initial condition constructions.

The method is similar to that used in [18,66]. The key idea consists of using $\ell = |m| = 2$ waveforms to compute the fitting factor between a given numerical relativity waveform, and an array of templates. In this work, we have assigned $f_{\rm ref} = 10$ Hz, which is at the lower end of the detectability range for LIGO. To estimate the eccentricity of our numerical relativity waveforms, we need to compute a few objects. The first of them is the inner product between one of our numerical relativity waveforms, $h_{22}^{\rm NR}$, and a waveform template, $h_{22}^{\rm template}$, given by:

$$\langle h_{22}^{\rm NR}|h_{22}^{\rm template}\rangle = \mathcal{R}\left[\int_{t_1}^{t_2} h_{22}^{\rm NR} h_{22}^{*\ \rm template}\right]. \tag{1}$$

Where $\mathcal{R}$ represents the real component. Note that the inner product is calculated by maximizing over both the time and phase of the two waveforms. t_1 represents an initial time at a point free from initial junk radiation, and t_2 marks the end of the numerical relativity simulation. t_2 in general is 50–100 M after merger for the signal to reach the outermost detectors in the simulation, but not long enough so that the initial junk radiation gets reflected back to the detectors due to the outer Dirichlet boundary conditions. The norm of a waveform is given by:

$$\|h\| \equiv \sqrt{\langle h|h\rangle}. \tag{2}$$

With these two quantities, we can compute the fitting factor between one of our numerical relativity waveforms and a bank of waveform templates, and thus measure the eccentricity e_0 as:

$$\mathrm{FF} \equiv \max_{t_0,\phi_0} \frac{\langle h_{22}^{\rm NR}|h_{22}^{\rm template}\rangle}{\|h_{22}^{\rm NR}\| \cdot \|h_{22}^{\rm template}\|}, \tag{3}$$

$$e_0 = \arg\max_{e_0}(\mathrm{FF}), \tag{4}$$

where the eccentricity e_0 is defined at the lower frequency bound $f_{\rm ref}$ which determines the length of the simulation prior to merger for the template. This calculation essentially corresponds to the inner product of a numerical relativity waveform maximized over a bank of SEOBNRE and EOBResumS templates. Note that to dimensionalize $f_{\rm ref}$, the total mass of the binary (M) needs to be provided. Thus, all inferences of eccentricity are dependent on the choice of M, which differed based on the waveform template code for stability purposes.

All inferred eccentricities for both TEOBResumS and SEOBNRE are given in Table I.

A. TEOBResumS inferences

For TEOBResumS waveforms (produced with the TEOBResumS-DALI branch), we set the total mass of the binary system $M = 30M_\odot$ and $f_{\rm ref} = 10$ Hz. Scans were made up to $e_0 = 0.8$, with a resolution of 0.001. To note, for TEOBResumS, the waveform begins from apastron and while we maximize the fitting factor by changing the initial phase ϕ_0, this resulting definition of $f_{\rm ref}$ is different from that used in SEOBNRE.

From Table I, we see that good matches are obtained for nearly all the simulations—23 out of 27 simulations have FF > 90%. The remaining simulations that do not match well visually appear to be of high eccentricity (possibly $e_0 > 0.8$) which would be beyond the explored parameter space. Figure 2 shows a comparison between the simulations and the best fitting TEOBResumS for 3 simulations.

B. SEOBNRE inferences

To produce this bank of SEOBNRE templates, we set $f_{\rm ref} = 10$ Hz. To obtain stable SEOBNRE waveforms, we set the total mass of the binary system $M = 60M_\odot$ for

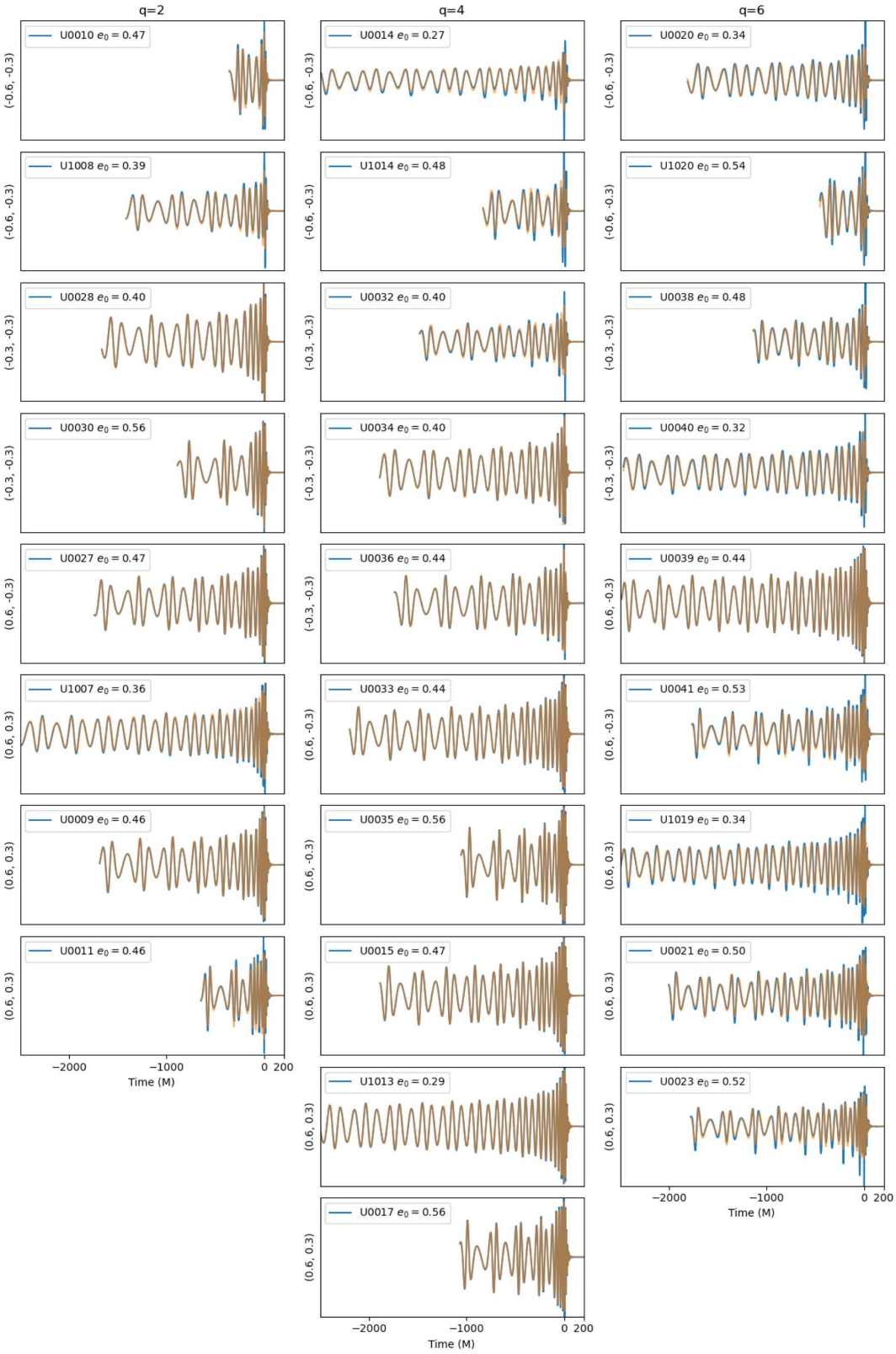

FIG. 1. *Numerical relativity waveform catalog* Each column is associated with a given mass-ratio $q = \{2, 4, 6\}$. From top to bottom, simulations are ordered in (χ_{1z}, χ_{2z}). The eccentricity e_0 inferred from `TEOBResumS` is given in the label. Each panel presents two types of waveforms: a $\ell = |m| = 2$ signal (orange), and one that includes higher order modes (blue). We have selected the inclination of the binary that maximizes the contribution higher order modes.

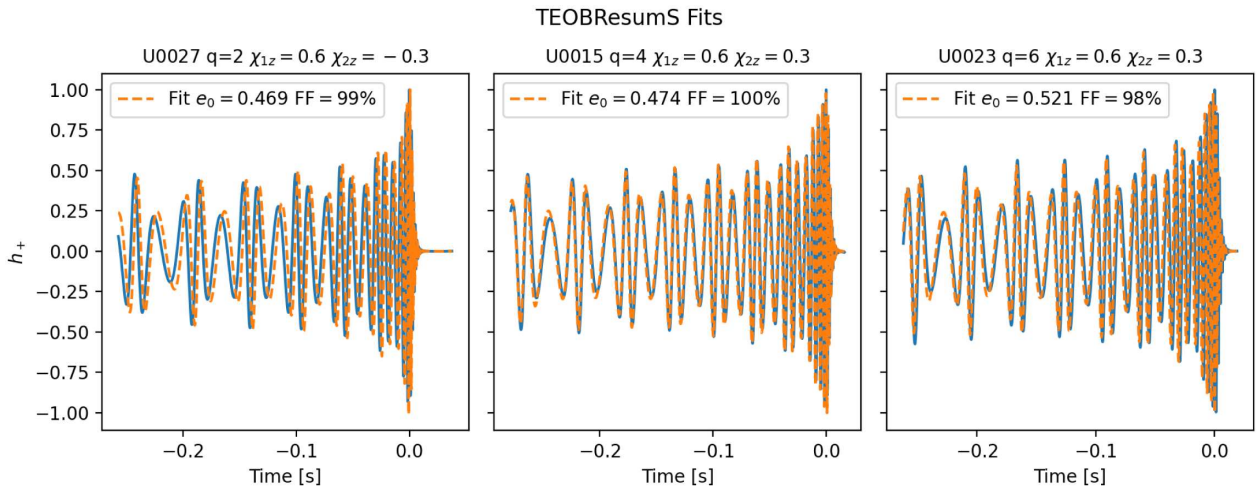

FIG. 2. *Comparison between numerical relativity waveforms and* `TEOBResumS`. Comparison of three waveforms overlaid with the best matching `TEOBResumS` waveform, effectively calibrating the eccentricity e_0 of the waveform. The total mass of the binary is $M = 30M_\odot$ and the reference frequency is $f_{\rm ref} = 10$ Hz. Solid lines represent numerical relativity waveforms, while dotted lines represent optimal `TEOBResumS` templates.

$e \leq 0.5$ and $M = 30M_\odot$ for $e > 0.5$. Higher mass binaries spend less cycles in the detectable frequency band, and so for highly eccentric simulations, the code does not have enough inspiral points to produce an accurate waveform, requiring a smaller mass for stability. Lower mass binaries at low eccentricities produced waveforms that were too large, and thus $M = 60M_\odot$ was chosen for efficiency.

As seen in Table I, we find good fitting factors for roughly half of the simulations. For some highly eccentric simulations, a suitable match was not found. This is because some numerical relativity waveforms contain moderately spinning binaries with highly eccentric orbits that are beyond the realm of applicability of the SEOBNRE model. It is possible to quantify the reliability of SEOBNRE signals with the "spin hang-up parameter", $\chi_{\rm up}$ [66]

$$\chi_{\rm up} = \frac{8\chi_{\rm eff} + 3\sqrt{1-4\eta}\chi_A}{11}, \tag{5}$$

where $\chi_{\rm eff} = (q\chi_{1z} + \chi_{2z})/(1+q)$, $\chi_A = (q\chi_{1z} - \chi_{2z})/(1+q)$ and $\eta = m_1 m_2/M^2$ for a binary of masses (m_1, m_2) and (orbit aligned) dimensionless spins (χ_{1z}, χ_{2z}) respectively. Furthermore, $M = m_1 + m_2$ and $q = m_1/m_2 \geq 1$.

For simulations with poor matches, we find that $\chi_{\rm up} > 0.35$, and visual inspection of these waveforms suggest high eccentricity, $e_0 > 0.6$. The SEOBNRE template waveform is inaccurate in producing reliable waveforms in that region of parameter space [66]. Indeed, for the two simulations with $\chi_{\rm up} = -0.5$, we were unable to obtain a suitable waveform. Nevertheless, in the valid regions, eccentricities are found to good accuracy. For simulations with FF $< 75\%$ the eccentricity is considered unconstrained, and we simply report the best match for completeness.

C. Comparison of the two waveform models

For a detailed comparison between the two waveform models, we refer to Knee *et al.* [68] which goes into detail about the systematic differences. Two results that can be corroborated is the fact that the `TEOBResumS` calibrated e_0 is uniformly less than that of `SEOBNRE` ($e_0^{\rm TEOB} < e_0^{\rm SEOBNRE}$). Moreover, the disparity is low at $e_0^{\rm TEOB} \approx 0.2$ and increases up to 50% for higher eccentricities.

IV. IMPORTANCE OF HIGHER ORDER HARMONICS

Having computed higher order wave modes, $h^{lm}(t)$, we can construct the full waveform

$$h(t,\theta,\phi) = h_+ + ih_\times = \sum_{l\geq 2}\sum_{m\geq -l}^{m\leq l} h^{lm}\,{}_{-2}Y_{lm}(\theta,\phi), \tag{6}$$

where ${}_{-2}Y_{lm}(\theta,\phi)$ are the spin-weight–2 spherical harmonics computed at a particular inclination (θ) and azimuth (ϕ). $\theta = 0$ corresponds to observing the binary face-on, i.e., with the orbital angular momentum vector pointed toward the observer.

Since nearly eccentric waveforms resemble quasicircular signals near merger due to circularization, we compute the importance of including higher order harmonics on the signal across the entire waveform evolution to better quantify the effect of eccentricity. From the results of [46] Sec. III, the $\Delta\mathcal{B}$ metric is used. It involves integrating over the entire numerical relativity waveform (after removing junk radiation)

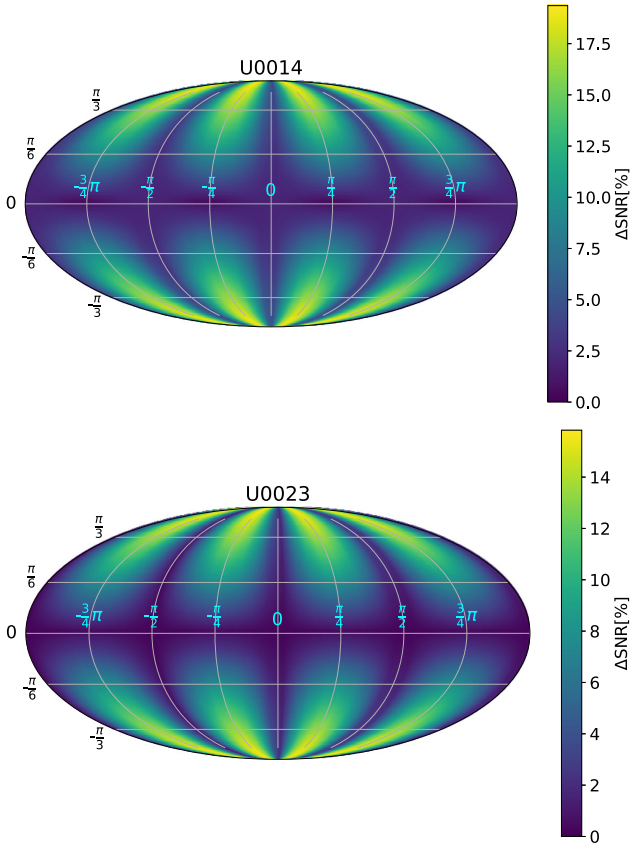

FIG. 3. *Importance of higher order modes for SNR calculations* The panels show the high increase in SNR, ΔSNR in Eq. (10), as a result of including higher order modes in the modeling of eccentric, spinning, binary black hole mergers. We assume an advanced LIGO-type detector, and binaries with total mass $M = 60M_\odot$ for numerical relativity waveform U0014 (top panel) and U0023 (bottom panel).

$$\mathcal{B}^{(l,|m|)}(\theta,\phi) = \int_{t=t_0}^{T} \sqrt{h(t,\theta,\phi)\tilde{h}(t,\theta,\phi)}\mathrm{d}t, \tag{7}$$

$$\Delta\mathcal{B}(\theta,\phi) = \frac{\mathcal{B}^{(\ell,|m|)}(\theta,\phi) - \mathcal{B}^{(\ell=|m|=2)}(\theta,\phi)}{\mathcal{B}^{(\ell=|m|=2)}(\hat{\theta},\hat{\phi})}, \tag{8}$$

where $(\hat{\theta},\hat{\phi})$ represent the orientation that maximizes the $(\ell = |m| = 2)$ mode of $\mathcal{B}$. To find the (θ,ϕ) combination that maximizes the contribution of higher order modes in terms of SNR calculations, we scan across (θ,ϕ) space at a resolution of 0.01 radians and select the orientation (θ^*,ϕ^*) that maximizes $\Delta\mathcal{B}$ in Eq. (8). The resultant optimal orientation is usually within three categories: one with the inclination close to the pole, one with inclination close to the equator and one slightly apart from both these angles.

To quantify the impact higher order modes would have on ground based detectors, we focus on the optimal SNR response of a waveform [**h**] as [46]

$$\mathrm{SNR}[\mathbf{h}]^2 = 4\mathcal{R}\int_0^\infty \frac{\tilde{h}(f)\tilde{h}^*(f)}{S_n(f)}\mathrm{d}f, \tag{9}$$

where $S_n(f)$ is the one-sided power spectral density (PSD) for LIGO's zero detuned high power configuration (ZDHP) [72]. We thus compute SNRs for both $(\ell,|m|)$ and $(\ell = |m| = 2)$ modes across all sky locations (α,β) with the optimized orientation (θ^*,ϕ^*). For the following results we set the polarization angle to $\psi = \pi/4$, and compute the effect of the higher order modes as

$$\Delta\mathrm{SNR} = \frac{\mathrm{SNR}^{(\ell,|m|)} - \mathrm{SNR}^{(\ell=|m|=2)}}{\hat{\mathrm{SNR}}^{(\ell=|m|=2)}}, \tag{10}$$

where $\hat{\mathrm{SNR}}^{(\ell=|m|=2)}$ is the maximum value of the $\ell = |m| = 2$ mode across the sky $(\hat{\alpha},\hat{\beta})$. The total mass of the binary is set to $M = 60M_\odot$.

The results can be categorized into three different categories depending on what the optimal orientation of the binary is (θ^*,ϕ^*). The first category is that in which $\theta^* \to 0$, and the inclusion of higher order modes has a marginal impact on the SNR of the signal, typically no more than 4%. The second category is for $70° < \theta^* < 110°$, in which case the contribution of higher order modes to the SNR of the signal is significant, with $\Delta\mathrm{SNR} \sim 25\%$. The final category are the in-between values of θ^* for which ΔSNR will be intermediate to that of the first two categories. Figure 3 shows the high effect of higher order modes on the skymap for two simulations. Increasing the mass of the binary to $M = 80M_\odot$ yields an increase of SNR to nearly 25% for some of the simulations.

These studies underscore the importance of including higher order modes in the modeling and detection of eccentric compact binary mergers, since SNR increases of order $\Delta\mathrm{SNR} \sim 20\%$ mean that marginally detectable signals [73] may then become easier to detect, or observable to larger distances.

V. COMPARISONS WITH QUASICIRCULAR WAVEFORMS

Studies in the literature have shown that the morphology of nonspinning, mildly eccentric binary black hole mergers may be captured by quasicircular, spinning, nonprecessing binary black hole mergers [7]. Here we quantify whether this parameter space degeneracy between orbital eccentricity and spin corrections still remain when we directly compare our new set of eccentric, spinning, nonprecessing numerical relativity waveforms with the `NRHybSur2dq8` surrogate model [74] that describes quasicircular, spinning, nonprecessing mergers.

We carry out this study by computing fitting factor calculations, see Eq. (3), between a given waveform in our numerical relativity catalog and an array of `NRHybSur2dq8` waveforms that scan the (q,χ_{1z},χ_{2z})

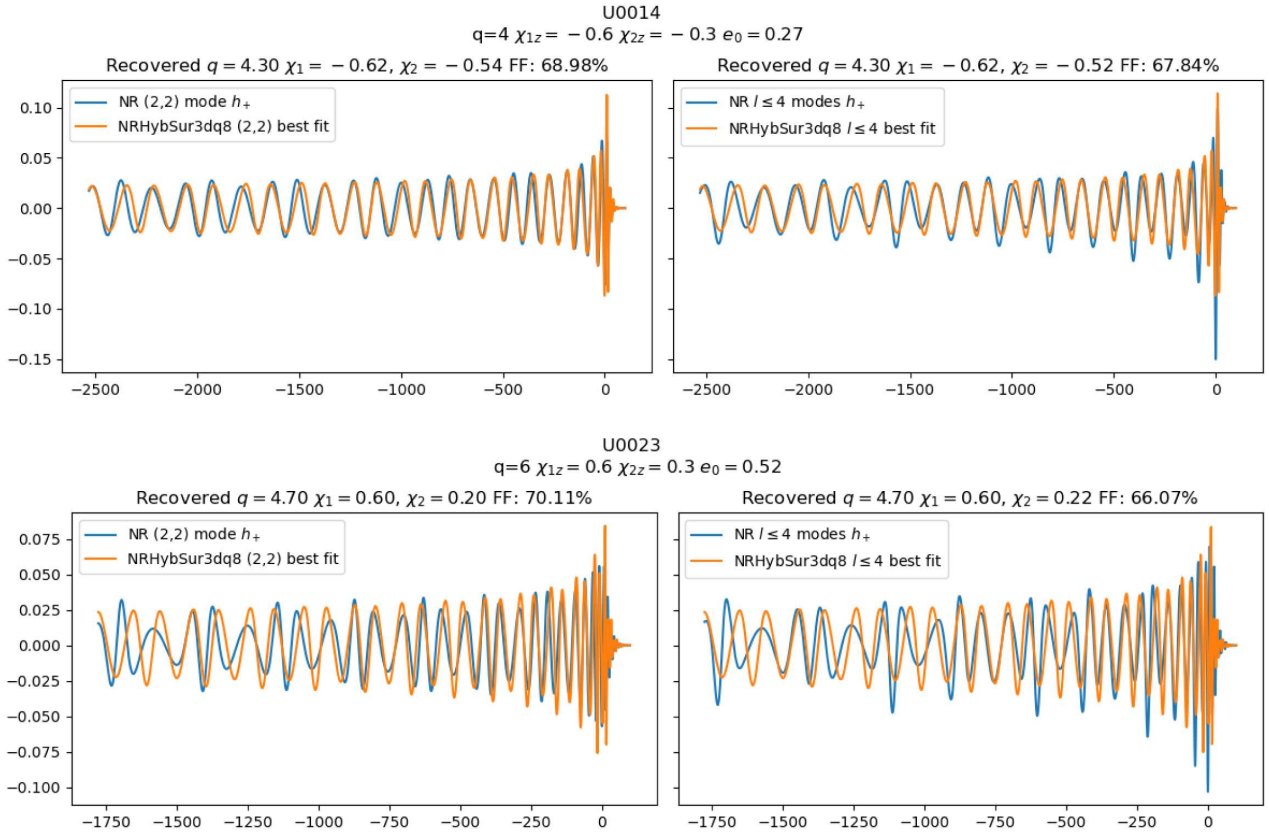

FIG. 4. *Nonparameter space degeneracy between spin and eccentricity corrections* Fitting factor (FF) calculations between numerical relativity waveform U0014 (top panels) and U0023 (bottom panels) and NRHybSur2dq8 waveform templates. In both cases, we show results for signals that include only $\ell = |m| = 2$ modes (left panels) and higher order modes (right panels). We notice significant discrepancies between ground-truth and recovered values for the mass-ratio and individual spins of the binary components through FF calculations.

parameter space using a simple grid search. We use an interval of size $\Delta q = 2$ centered around the truth mass-ratio. So for numerical relativity waveforms of mass-ratio $q = 4$, we scan an interval that covers the range $2 \leq q \leq 6$ (note for $q = 2$ the interval is $1 \leq q \leq 4$). For individual spins, we consider the range $-0.7 \leq \chi_{\{1z,2z\}} \leq 0.7$. The resolution of the search is $\delta q = 0.1$, and $\delta\chi = 0.02$ for both spins. Following these conventions, we consider two cases. In the first both numerical relativity waveforms and `NRHybSur2dq8` waveforms include only the $\ell = |m| = 2$ mode, whereas in the second case both types of waveforms include higher order modes. Results of this analysis for simulations U0014 and U0023 are presented in Fig. 4.

Additional results for other numerical simulations in our waveform catalog may be found in Table II. These findings, along with the results we presented in Table I using the SEOBNRE waveform family, exhibit the importance of developing waveform models that are informed by numerical relativity simulations to accurately capture orbital eccentricity and spin corrections. At this time, these results show that moderately or highly eccentric and spinning signals may not be captured by template matching algorithms, unless the signal is loud enough to be captured by unmodeled (burst) searches.

In summary, this study shows that it is not possible for quasicircular, spinning, nonprecessing signals to capture the dynamics of moderately and highly eccentric, spinning, nonprecessing signals. We either develop the required methods (waveforms and signal processing tools) to search for and find these signals or we may miss an interesting population of compact binary sources.

VI. CONCLUSIONS

We have presented a set of 27 eccentric, spin-aligned binary black hole simulations that describe three different mass-ratios $q = \{2, 4, 6\}$. To measure the eccentricity of the simulations, we computed fitting factors against two spin-aligned eccentric effective-one-body models with eccentricity—`TEOBResumS` and `SEOBNRE`. We were able to estimate eccentricities for nearly all of the simulations with `TEOBResumS`, with eccentricity ranges of $0.27 \leq e_0^{\mathrm{TEOB}} < 0.58$ and roughly half of the simulations with `SEOBNRE` with eccentricity ranges $0.26 \leq e_0^{\mathrm{SEOBNRE}} < 0.8$. The remaining simulations appear to be of even higher

eccentricity, though producing such waveforms from templates proved to be difficult for the values of spins and orbital eccentricities used in our simulations. Current limitations to the existing SEOBNRE library will be alleviated by including higher order eccentricity terms, which become increasingly important at higher mass ratios as indicated by our findings and those reported in [66]. Indeed in Liu *et al.* [67], the authors introduce a new model `SEOBNREHM` that utilizes these higher order terms greatly that improves fitting factors and produces accurate waveforms for maximally spinning, highly eccentric simulations. Comparing our simulations with this model is a future project that may yield new results.

For these simulations, we performed the following analyses:

(1) Selecting the orientation of the binary that maximizes the contribution of higher order modes, we computed the SNR observed for ground-based LIGO-type detectors across the sky. In doing so, we observed that for simulations, the inclusion of high order modes in the waveform increases the SNR between 5%–35%.
(2) We do not find significant parameter space degeneracies between spinning, eccentric waveforms and quasicircular, spinning waveforms upon computing fitting factor calculations assuming a coarse grid search across mass ratio, and spins. In general the fitting factors are worse when comparing higher order modes.

These analyses underscore the importance of using numerical relativity to understand the physics of these compact binary systems, and then inform the design of neural network models [46,48,75,76], matched filtering approaches [77,78], or unmodeled searches [79,80] to discover moderately and highly eccentric spinning binaries in future discovery campaigns.

We also found that including higher order terms will enhance the detectability as the results suggest that the $(\ell = |m| = 2)$ modes do not faithfully capture the dynamics of the system for asymmetric mass-ratio systems.

This set of simulations extends the library of open-source simulations introduced in [3], stored in the DataVault repository maintained by NCSA at the University of Illinois [81]. We intend to make this set of simulations publicly available on the same repository soon and until then, any data can be availed upon request to the authors of this paper.

ACKNOWLEDGMENTS

We thank the anonymous reviewer for their comments and suggestions, we thank Rossella Gamba for help in setting up the `TEOBResumS` model. This material is based upon work supported by the National Science Foundation under Grants No. NSF-2004879, No. NSF-1550514, No. ACI-1238993. Numerical simulations used compute resources provided by XSEDE under allocation No. TG-PHY160053. E. A. H. gratefully acknowledges support from NSF award No. OAC-1931561. This material is based upon work supported by Laboratory Directed Research and Development (LDRD) funding from Argonne National Laboratory, provided by the Director, Office of Science, of the U.S. Department of Energy under Contract No. DE-AC02-06CH11357. Plots were produced using matplotlib [82,83]. Part of the analysis was parallelized using TACC's launcher utility [84].

APPENDIX A: CONVERGENCE

Details about the nature of convergence can be found in appendix B of [3]. To summarize, though the spatial finite difference operators are at 8th order, the error in the simulations does not scale to 8th order with spatial resolution. This is due to a combination of lower order operations due interpolation on the mesh refinement boundary (5th order accuracy), adaptive mesh refinement operations and varying temporal resolution (from differing spatial resolutions). For each simulation in the library, we have 3 different resolutions which we use to check for convergence—$N = 36$, 40, 44 corresponding to the number of points in the finest grid radius. We compare the phase difference between the highest resolution and the lower resolutions. To see how much the phase difference reduces with resolution, we scale the phase difference of the higher difference $(h_{40}–h_{44})$ to match the lower difference $(h_{36}–h_{44})$. Figure 5 shows the phase difference of the signals for the U1007 simulation. The order appears to be around 7 which is reasonable for these simulations. Note that this is not the

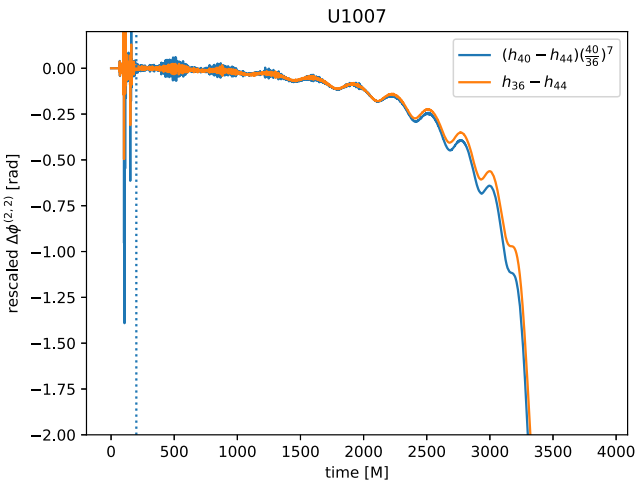

FIG. 5. Convergence of the phase difference between the waveform of the highest resolution (h_{44}) and the lower resolutions (h_{40}, h_{36}) with appropriate scaling to get a rough match. This suggests an order of around 7 but this is not representative of the entire library. Note that the plot includes the initial junk radiation (left of vertical dotted line) and the merger and ringdown signal both of which have very large phase differences that are cut out in the plot.

TABLE II. Parameters from NRHybSur2dq8 that best match the simulation data along with fitting factors (FFs) for both ($\ell = |m| = 2$) and the $l \leq 4$ modes. Low FFs indicate that spin-aligned eccentric signals, such as those in our simulation library, will be poorly recovered or go missing when using current quasicircular template match filtering techniques. The only chance to see these signals would be through unmodeled searches if they are sufficiently loud.

	$\ell = m = 2$				$l \leq 4$			
Simulation	q	χ_{1z}	χ_{2z}	FF(%)	q	χ_{1z}	χ_{2z}	FF(%)
U0010	2.7	0.60	−0.53	60.9	2.3	0.55	0.37	46.7
U0011	3.0	0.58	0.28	47.8	1.1	0.13	0.54	49.8
U0014	4.3	−0.62	−0.54	69.0	4.3	−0.62	−0.52	67.8
U0020	6.0	−0.62	−0.56	84.9	5.2	−0.6	−0.09	82.5
U0021	5.4	0.60	−0.31	52.5	5.7	0.47	0.58	48.5
U0023	4.7	0.60	0.20	70.1	4.7	0.60	0.22	66.1
U1007	1.4	0.56	0.66	93.9	1.3	0.58	0.66	93.9
U1008	1.4	−0.49	−0.56	80.2	1.0	−0.52	−0.43	79.3
U1019	5.6	0.60	0.35	90.8	5.5	0.60	0.51	90.0
U0032	5.0	−0.62	0.28	40.0	4.5	−0.51	−0.23	39.6
U0038	5.0	−0.58	−0.17	39.5	6.8	−0.47	−0.66	42.0
U0040	5.7	−0.33	−0.05	88.4	5.2	−0.20	−0.64	85.7
U0041	5.0	0.47	0.01	62.1	5.0	0.47	−0.15	55.5

same scaling for other simulations in the library—it can vary from 4 to 10. This illustrates the point that it is difficult to pull out a universal convergence scaling of the simulations.

APPENDIX B: INFERRED PARAMETERS FROM NRHybSur2dq8

Here we list the inferred parameters from the parameter survey of the NRHybSur2dq8 library of quasicircular, spin-aligned binary waveforms for both the ($\ell = |m| = 2$) and the $l \leq 4$ modes separately. The simulations not listed in Table II had consistently low FFs across all parameter space. The resolution of the grid search was 0.1 in q, and 0.02 in spins near the inferred values (a lower resolution search was initially done followed by a finer search).

[1] B. Moore, T. Robson, N. Loutrel, and N. Yunes, A Fourier domain waveform for nonspinning binaries with arbitrary eccentricity, Classical Quantum Gravity **35**, 235006 (2018).

[2] A. Ramos-Buades, S. Husa, G. Pratten, H. Estellés, C. García-Quirós, M. Mateu-Lucena, M. Colleoni, and R. Jaume, First survey of spinning eccentric black hole mergers: Numerical relativity simulations, hybrid waveforms, and parameter estimation, Phys. Rev. D **101**, 083015 (2020).

[3] E. A. Huerta, R. Haas, S. Habib, A. Gupta, A. Rebei, V. Chavva, D. Johnson, S. Rosofsky, E. Wessel, B. Agarwal, D. Luo, and W. Ren, Physics of eccentric binary black hole mergers: A numerical relativity perspective, Phys. Rev. D **100**, 064003 (2019).

[4] I. Hinder, L. E. Kidder, and H. P. Pfeiffer, Eccentric binary black hole inspiral-merger-ringdown gravitational waveform model from numerical relativity and post-Newtonian theory, Phys. Rev. D **98**, 044015 (2018).

[5] Z. Cao and W.-B. Han, Waveform model for an eccentric binary black hole based on the effective-one-body-numerical-relativity formalism, Phys. Rev. D **96**, 044028 (2017).

[6] T. Hinderer and S. Babak, Foundations of an effective-one-body model for coalescing binaries on eccentric orbits, Phys. Rev. D **96**, 104048 (2017).

[7] E. A. Huerta, C. J. Moore, P. Kumar, D. George, A. J. K. Chua, R. Haas, E. Wessel, D. Johnson, D. Glennon, A. Rebei, A. M. Holgado, J. R. Gair, and H. P. Pfeiffer, Eccentric, nonspinning, inspiral, Gaussian-process merger approximant for the detection and characterization of eccentric binary black hole mergers, Phys. Rev. D **97**, 024031 (2018).

[8] Z. Chen, E. A. Huerta, J. Adamo, R. Haas, E. O'Shea, P. Kumar, and C. Moore, Observation of eccentric binary black hole mergers with second and third generation gravitational wave detector networks, Phys. Rev. D **103**, 084018 (2021).

[9] E. A. Huerta, P. Kumar, B. Agarwal, D. George, H.-Y. Schive, H. P. Pfeiffer, R. Haas, W. Ren, T. Chu, M. Boyle, D. A. Hemberger, L. E. Kidder, M. A. Scheel, and B. Szilagyi, Complete waveform model for compact binaries on eccentric orbits, Phys. Rev. D **95**, 024038 (2017).

[10] T. Osburn, N. Warburton, and C. R. Evans, Highly eccentric inspirals into a black hole, Phys. Rev. D **93**, 064024 (2016).

[11] N. Loutrel and N. Yunes, Hereditary effects in eccentric compact binary inspirals to third post-Newtonian order, Classical Quantum Gravity **34**, 044003 (2017).
[12] N. Loutrel and N. Yunes, Eccentric gravitational wave bursts in the post-Newtonian formalism, Classical Quantum Gravity **34**, 135011 (2017).
[13] I. Hinder, B. Vaishnav, F. Herrmann, D. M. Shoemaker, and P. Laguna, Circularization and final spin in eccentric binary-black-hole inspirals, Phys. Rev. D **77**, 081502 (2008).
[14] D. Bini, T. Damour, and A. Geralico, High post-Newtonian order gravitational self-force analytical results for eccentric equatorial orbits around a Kerr black hole, Phys. Rev. D **93**, 124058 (2016).
[15] C. Kavanagh, D. Bini, T. Damour, S. Hopper, A. C. Ottewill, and B. Wardell, Spin-orbit precession along eccentric orbits for extreme mass ratio black hole binaries and its effective-one-body transcription, Phys. Rev. D **96**, 064012 (2017).
[16] J. Levin, S. T. McWilliams, and H. Contreras, Inspiral of generic black hole binaries: Spin, precession and eccentricity, Classical Quantum Gravity **28**, 175001 (2011).
[17] E. A. Huerta, P. Kumar, S. T. McWilliams, R. O'Shaughnessy, and N. Yunes, Accurate and efficient waveforms for compact binaries on eccentric orbits, Phys. Rev. D **90**, 084016 (2014).
[18] S. Habib and E. A. Huerta, Characterization of numerical relativity waveforms of eccentric binary black hole mergers, Phys. Rev. D **100**, 044016 (2019).
[19] E. A. Huerta and D. A. Brown, Effect of eccentricity on binary neutron star searches in Advanced LIGO, Phys. Rev. D **87**, 127501 (2013).
[20] N. Yunes, K. G. Arun, E. Berti, and C. M. Will, Post-circular expansion of eccentric binary inspirals: Fourier-domain waveforms in the stationary phase approximation, Phys. Rev. D **80**, 084001 (2009).
[21] S. Habib, A. Ramos-Buades, E. A. Huerta, S. Husa, R. Haas, and Z. Etienne, Initial data and eccentricity reduction Toolkit for binary black hole numerical relativity waveforms, Classical Quantum Gravity **38**, 125007 (2021).
[22] M. Coughlin, P. Meyers, E. Thrane, J. Luo, and N. Christensen, Detectability of eccentric compact binary coalescences with advanced gravitational-wave detectors, Phys. Rev. D **91**, 063004 (2015).
[23] B. Moore, M. Favata, K. G. Arun, and C. Kant Mishra, Gravitational-wave phasing for low-eccentricity inspiralling compact binaries to 3PN order, Phys. Rev. D **93**, 124061 (2016).
[24] K. S. Tai, S. T. McWilliams, and F. Pretorius, Detecting gravitational waves from highly eccentric compact binaries, Phys. Rev. D **90**, 103001 (2014).
[25] C. M. Will, Capture of non-relativistic particles in eccentric orbits by a Kerr black hole, Classical Quantum Gravity **29**, 217001 (2012).
[26] S. Tanay, M. Haney, and A. Gopakumar, Frequency and time-domain inspiral templates for comparable mass compact binaries in eccentric orbits, Phys. Rev. D **93**, 064031 (2016).
[27] J. Samsing and E. Ramirez-Ruiz, On the assembly rate of highly eccentric binary black hole mergers, Astrophys. J. Lett. **840**, L14 (2017).
[28] V. Gayathri, J. Healy, J. Lange, B. O'Brien, M. Szczepanczyk, I. Bartos, M. Campanelli, S. Klimenko, C. O. Lousto, and R. O'Shaughnessy, Eccentricity estimate for black hole mergers with numerical relativity simulations, Nat. Astron. **6**, 344 (2022).
[29] B.-M. Hoang, S. Naoz, B. Kocsis, F. A. Rasio, and F. Dosopoulou, Black hole mergers in galactic nuclei induced by the eccentric Kozai-Lidov effect, Astrophys. J. **856**, 140 (2018).
[30] L. Gondán and B. Kocsis, Measurement accuracy of inspiraling eccentric neutron star and black hole binaries using gravitational waves, Astrophys. J. **871**, 178 (2019).
[31] L. Gondán, B. Kocsis, P. Raffai, and Z. Frei, Accuracy of estimating highly eccentric binary black hole parameters with gravitational-wave detections, Astrophys. J. **855**, 34 (2018).
[32] T. Islam, V. Varma, J. Lodman, S. E. Field, G. Khanna, M. A. Scheel, H. P. Pfeiffer, D. Gerosa, and L. E. Kidder, Eccentric binary black hole surrogate models for the gravitational waveform and remnant properties: Comparable mass, nonspinning case, Phys. Rev. D **103**, 064022 (2021).
[33] C. L. Rodriguez, P. Amaro-Seoane, S. Chatterjee, K. Kremer, F. A. Rasio, J. Samsing, C. S. Ye, and M. Zevin, Post-Newtonian dynamics in dense star clusters: Formation, masses, and merger rates of highly-eccentric black hole binaries, Phys. Rev. D **98**, 123005 (2018).
[34] M. Zevin, J. Samsing, C. Rodriguez, C.-J. Haster, and E. Ramirez-Ruiz, Eccentric black hole mergers in dense star clusters: The role of binary-binary encounters, Astrophys. J. **871**, 91 (2019).
[35] J. Samsing, Eccentric black hole mergers forming in globular clusters, Phys. Rev. D **97**, 103014 (2018).
[36] J. Samsing, Eccentric black hole mergers forming in globular clusters, Phys. Rev. D **97**, 103014 (2018).
[37] L. Chomiuk, J. Strader, T. J. Maccarone, J. C. A. Miller-Jones, C. Heinke, E. Noyola, A. C. Seth, and S. Ransom, A radio-selected black hole x-ray binary candidate in the milky way globular cluster M62, Astrophys. J. **777**, 69 (2013).
[38] J. Strader, L. Chomiuk, T. J. Maccarone, J. C. A. Miller-Jones, and A. C. Seth, Two stellar-mass black holes in the globular cluster M22, Nature (London) **490**, 71 (2012).
[39] M. Gieles, D. Erkal, F. Antonini, E. Balbinot, and J. Peñarrubia, A supra-massive population of stellar-mass black holes in the globular cluster Palomar 5, Nat. Astron. **5**, 957 (2021).
[40] B. Kocsis and J. Levin, Repeated bursts from relativistic scattering of compact objects in galactic nuclei, Phys. Rev. D **85**, 123005 (2012).
[41] R. M. O'Leary, B. Kocsis, and A. Loeb, Gravitational waves from scattering of stellar-mass black holes in galactic nuclei, Mon. Not. R. Astron. Soc. **395**, 2127 (2009).
[42] N. W. C. Leigh, A. M. Geller, B. McKernan, K. E. S. Ford, M. M. Mac Low, J. Bellovary, Z. Haiman, W. Lyra, J. Samsing, M. O'Dowd, B. Kocsis, and S. Endlich, On the rate of black hole binary mergers in galactic nuclei due to dynamical hardening, Mon. Not. R. Astron. Soc. **474**, 5672 (2018).

[43] V. Tiwari, S. Klimenko, N. Christensen, E. A. Huerta, S. R. P. Mohapatra, A. Gopakumar, M. Haney, P. Ajith, S. T. McWilliams, G. Vedovato, M. Drago, F. Salemi, G. A. Prodi, C. Lazzaro, S. Tiwari, G. Mitselmakher, and F. Da Silva, Proposed search for the detection of gravitational waves from eccentric binary black holes, Phys. Rev. D **93**, 043007 (2016).
[44] I. M. Romero-Shaw, P. D. Lasky, and E. Thrane, Searching for eccentricity: Signatures of dynamical formation in the first gravitational-wave transient catalogue of LIGO and Virgo, Mon. Not. R. Astron. Soc. **490**, 5210 (2019).
[45] A. H. Nitz, A. Lenon, and D. A. Brown, Search for eccentric binary neutron star mergers in the first and second observing runs of Advanced LIGO, Astrophys. J. **890**, 1 (2019).
[46] A. Rebei, E. A. Huerta, S. Wang, S. Habib, R. Haas, D. Johnson, and D. George, Fusing numerical relativity and deep learning to detect higher-order multipole waveforms from eccentric binary black hole mergers, Phys. Rev. D **100**, 044025 (2019).
[47] B. Abbott *et al.* (LIGO Scientific and Virgo Collaborations), Search for eccentric binary black hole mergers with Advanced LIGO and Advanced Virgo during their first and second observing runs, Astrophys. J. **883**, 149 (2019).
[48] W. Wei, E. A. Huerta, M. Yun, N. Loutrel, M. A. Shaikh, P. Kumar, R. Haas, and V. Kindratenko, Deep learning with quantized neural networks for gravitational-wave forecasting of eccentric compact binary coalescence, Astrophys. J. **919**, 82 (2021).
[49] I. Romero-Shaw, P. D. Lasky, and E. Thrane, Four eccentric mergers increase the evidence that LIGO-Virgo-KAGRA's binary black holes form dynamically, Astrophys. J. **940**, 171 (2022).
[50] R. Abbott *et al.* (LIGO Scientific and Virgo Collabortions), GW190521: A Binary Black Hole Merger with a Total Mass of 150 $M_\odot$, Phys. Rev. Lett. **125**, 101102 (2020).
[51] I. Romero-Shaw, P. D. Lasky, E. Thrane, and J. Calderón Bustillo, GW190521: Orbital eccentricity and signatures of dynamical formation in a binary black hole merger signal, Astrophys. J. Lett. **903**, L5 (2020).
[52] J. Samsing, I. Bartos, D. J. D'Orazio, Z. Haiman, B. Kocsis, N. W. C. Leigh, B. F. Liu, M. E. Pessah, and H. Tagawa, AGN as potential factories for eccentric black hole mergers, Nature (London) **603**, 237 (2022).
[53] J. Aasi *et al.* (The LIGO Scientific Collaboration), Advanced LIGO, Classical Quantum Gravity **32**, 074001 (2015).
[54] B. P. Abbott *et al.* (LIGO Scientific and Virgo Collaborations), Binary Black Hole Mergers in the First Advanced LIGO Observing Run, Phys. Rev. X **6**, 041015 (2016); **8**, 039903(E) (2018).
[55] F. Acernese *et al.* (The Virgo Collaboration), Advanced Virgo: A second-generation interferometric gravitational wave detector, Classical Quantum Gravity **32**, 024001 (2015).
[56] T. Akutsu, M. Ando, K. Arai *et al.*, Overview of KAGRA: Detector design and construction history, Prog. Theor. Exp. Phys. **2021**, 05A101 (2020).
[57] F. Löffler, J. Faber, E. Bentivegna, T. Bode, P. Diener, R. Haas, I. Hinder, B. C. Mundim, C. D. Ott, E. Schnetter, G. Allen, M. Campanelli, and P. Laguna, The EINSTEIN TOOLKIT: A community computational infrastructure for relativistic astrophysics, Classical Quantum Gravity **29**, 115001 (2012).
[58] T. Damour and A. Nagar, New effective-one-body description of coalescing nonprecessing spinning black-hole binaries, Phys. Rev. D **90**, 044018 (2014).
[59] A. Nagar, T. Damour, C. Reisswig, and D. Pollney, Energetics and phasing of nonprecessing spinning coalescing black hole binaries, Phys. Rev. D **93**, 044046 (2016).
[60] A. Nagar *et al.*, Time-domain effective-one-body gravitational waveforms for coalescing compact binaries with nonprecessing spins, tides, and self-spin effects, Phys. Rev. D **98**, 104052 (2018).
[61] A. Nagar, G. Pratten, G. Riemenschneider, and R. Gamba, Multipolar effective one body model for nonspinning black hole binaries, Phys. Rev. D **101**, 024041 (2020).
[62] A. Nagar, G. Riemenschneider, G. Pratten, P. Rettegno, and F. Messina, Multipolar effective one body waveform model for spin-aligned black hole binaries, Phys. Rev. D **102**, 024077 (2020).
[63] G. Riemenschneider, P. Rettegno, M. Breschi, A. Albertini, R. Gamba, S. Bernuzzi, and A. Nagar, Assessment of consistent next-to-quasicircular corrections and postadiabatic approximation in effective-one-body multipolar waveforms for binary black hole coalescences, Phys. Rev. D **104**, 104045 (2021).
[64] D. Chiaramello and A. Nagar, Faithful analytical effective-one-body waveform model for spin-aligned, moderately eccentric, coalescing black hole binaries, Phys. Rev. D **101**, 101501 (2020).
[65] A. Nagar, A. Bonino, and P. Rettegno, Effective one-body multipolar waveform model for spin-aligned, quasicircular, eccentric, hyperbolic black hole binaries, Phys. Rev. D **103**, 104021 (2021).
[66] X. Liu, Z. Cao, and L. Shao, Validating the effective-one-body numerical-relativity waveform models for spin-aligned binary black holes along eccentric orbits, Phys. Rev. D **101**, 044049 (2020).
[67] X. Liu, Z. Cao, and Z.-H. Zhu, A higher-multipole gravitational waveform model for an eccentric binary black holes based on the effective-one-body-numerical-relativity formalism, Classical Quantum Gravity **39**, 035009 (2022).
[68] A. M. Knee, I. M. Romero-Shaw, P. D. Lasky, J. McIver, and E. Thrane, A Rosetta Stone for eccentric gravitational waveform models, Astrophys. J. **936**, 172 (2022).
[69] V. Varma, S. E. Field, M. A. Scheel, J. Blackman, L. E. Kidder, and H. P. Pfeiffer, Surrogate model of hybridized numerical relativity binary black hole waveforms, Phys. Rev. D **99**, 064045 (2019).
[70] D. Johnson, E. A. Huerta, and R. Haas, Python Open source Waveform ExtractoR (POWER): An open source, PYTHON package to monitor and post-process numerical relativity simulations, Classical Quantum Gravity **35**, 027002 (2018).
[71] M. Favata, The gravitational-wave memory effect, Classical Quantum Gravity **27**, 084036 (2010).
[72] L. Barsotti, S. Gras, M. Evans, and P. Fritschel, Advanced LIGO anticipated sensitivity curves (2018), https://dcc.ligo.org/LIGO-T1800044/public.

[73] D. A. Brown, P. Kumar, and A. H. Nitz, Template banks to search for low-mass binary black holes in advanced gravitational-wave detectors, Phys. Rev. D **87**, 082004 (2013).
[74] V. Varma, S. E. Field, M. A. Scheel, J. Blackman, L. E. Kidder, and H. P. Pfeiffer, Surrogate model of hybridized numerical relativity binary black hole waveforms, Phys. Rev. D **99**, 064045 (2019).
[75] W. Wei and E. A. Huerta, Deep learning for gravitational wave forecasting of neutron star mergers, Phys. Lett. B **816**, 136185 (2021).
[76] M. B. Schäfer *et al.*, MLGWSC-1: The first machine learning gravitational-wave search mock data challenge, Phys. Rev. D **107**, 023021 (2023).
[77] S. A. Usman *et al.*, The PyCBC search for gravitational waves from compact binary coalescence, Classical Quantum Gravity **33**, 215004 (2016).
[78] S. Sachdev *et al.*, The GstLAL search analysis methods for compact binary mergers in Advanced LIGO's second and Advanced Virgo's first observing runs, arXiv:1901.08580.
[79] S. Klimenko, I. Yakushin, A. Mercer, and G. Mitselmakher, A coherent method for detection of gravitational wave bursts, Classical Quantum Gravity **25**, 114029 (2008).
[80] S. Klimenko, G. Vedovato, M. Drago, F. Salemi, V. Tiwari, G. A. Prodi, C. Lazzaro, K. Ackley, S. Tiwari, C. F. Da Silva, and G. Mitselmakher, Method for detection and reconstruction of gravitational wave transients with networks of advanced detectors, Phys. Rev. D **93**, 042004 (2016).
[81] Y. Luo, R. Haas, Q. Zhang, and G. Allen, DataVault: A data storage infrastructure for the EINSTEIN TOOLKIT, Classical Quantum Gravity **38**, 135016 (2021).
[82] J. D. Hunter, Matplotlib: A 2D graphics environment, Comput. Sci. Eng. **9**, 90 (2007).
[83] T. A. Caswell *et al.*, matplotlib/matplotlib: Rel: v3.4.3 (2021).
[84] L. A. Wilson and J. M. Fonner, Launcher: A shell-based framework for rapid development of parallel parametric studies, in *Proceedings of the 2014 Annual Conference on Extreme Science and Engineering Discovery Environment, XSEDE '14* (ACM, New York, NY, USA, 2014), pp. 40:1–40:8.